AGU PUBLICATIONS

JGR

Journal of Geophysical Research: Solid Earth

RESEARCH ARTICLE
10.1002/2013JB010616

Key Points:
- Melting relations and chemical compositions of melt and solid to CMB conditions
- Partial melt become more ultrabasic with increasing pressure
- Strong Fe enrichment in partial melts formed at deep lower mantle

Supporting Information:
- Readme
- Figure S1

Correspondence to:
S. Tateno,
tateno.s.aa@m.titech.ac.jp

Citation:
Tateno, S., K. Hirose, and Y. Ohishi (2014), Melting experiments on peridotite to lowermost mantle conditions, *J. Geophys. Res. Solid Earth*, *119*, 4684–4694, doi:10.1002/2013JB010616.

Received 19 AUG 2013
Accepted 30 MAY 2014
Accepted article online 3 JUN 2014
Published online 24 JUN 2014

Melting experiments on peridotite to lowermost mantle conditions

Shigehiko Tateno[1,2], Kei Hirose[2], and Yasuo Ohishi[3]

[1]Department of Earth and Planetary Sciences, Tokyo Institute of Technology, Meguro, Tokyo, Japan, [2]Earth-Life Science Institute, Tokyo Institute of Technology, Meguro, Tokyo, Japan, [3]Japan Synchrotron Radiation Research Institute, Sayo-cho, Hyogo, Japan

Abstract Melting experiments on a pyrolitic mantle material were performed in a pressure range from 34 to 179 GPa based on laser-heated diamond-anvil cell (DAC) techniques. The textural and chemical characterizations of quenched samples were made by using field-emission-type electron microprobe (FE-EPMA). Melts formed by 46 to 77 wt.% partial melting in this study were ultrabasic in composition and became more depleted in SiO_2 and more enriched in FeO with increasing pressure. Melting textures indicate that the liquidus phase changed from ferropericlase to $MgSiO_3$-rich perovskite at least above 34 GPa and further to post-perovskite. The first phase to melt (disappear) changed from $CaSiO_3$ perovskite to (Mg,Fe)O ferropericlase between 68 and 82 GPa. The stability of ferropericlase above solidus temperature shrinks with increasing pressure (melting last below 34 GPa and first 82 GPa), resulting in higher $(MgO + FeO)/SiO_2$ ratio in partial melt at higher pressure. Additionally, the Fe-Mg distribution coefficients (K_D) between perovskite/post-perovskite and melt decreased considerably with increasing pressure, leading to strong Fe-enrichment in partial melts. It supports dense partial melts in a deep lower mantle, which migrate downward to the core mantle boundary (CMB).

1. Introduction

Melting is a primary mechanism of chemical evolution of our planet. The Earth's mantle was likely to be completely molten right after the moon-forming giant impact [*Canup*, 2004]. Subsequent crystallization of a global magma ocean may have formed strong chemical stratification in the mantle. The seismic ultralow-velocity zones (ULVZs) suggest the presence of partial melts near the base of the mantle even at present [*Garnero and Helmberger*, 1995; *Lay et al.*, 2004], which might be the remnants of a basal magma ocean [*Labrosse et al.*, 2007]. The knowledge of melting phase relations and partial melt compositions in the lower mantle is crucial to understand the chemical evolution in the early Earth and the nature of ULVZs. Melting of peridotite has been extensively studied by using multi-anvil apparatus up to 33 GPa corresponding to the uppermost lower mantle conditions [*Zhang and Hertzberg*, 1994; *Hirose and Fei*, 2002; *Trønnes and Frost*, 2002; *Hirose et al.*, 2004; *Ito et al.*, 2004; *Walter et al.*, 2004]. However, melting experiments under the middle to deep lower mantle conditions are limited [*Fiquet et al.*, 2010; *Andrault et al.*, 2011].

Additionally, the density relationship between melt and co-existing solid is key for the fate of partial melts. Shockwave experiments and ab initio calculations consistently demonstrated that $MgSiO_3$ liquid is less dense than $MgSiO_3$ perovskite at the CMB [*Stixrude and Karki*, 2005; *Mosenfelder et al.*, 2009]. However, the melt-solid density crossover can occur depending on the partitioning of iron [*Stixrude et al.*, 2009]. Melting experiments on $(Mg_{0.89}Fe_{0.11})_2SiO_4$ bulk composition performed by *Nomura et al.* [2011] demonstrated on the basis of ex situ sample characterizations of melting texture and chemical composition that strong Fe enrichment occurred in partial melts above 75 GPa, indicating that melt is denser than solids in a middle to deep lower mantle. In contrast, more recent experiments by *Andrault et al.* [2012] based on in situ X-ray fluorescence (XRF) analyses found only small Fe enrichment in partial melts in a chondritic mantle bulk composition, suggesting that melt is less dense and floats upward to shallower depths.

Here we carried out the melting experiments on a pyrolitic mantle (KLB-1 peridotite) to deep lower mantle conditions up to 179 GPa by a combination of laser-heated DAC experiments and chemical analyses of recovered samples using a field-emission-type electron microprobe (FE-EPMA) with a high spatial resolution. On the basis of melting texture and chemical composition, we show melting sequence, partial melt composition, and solid-melt partitioning including the Fe-Mg distribution coefficient, K_D, between perovskite/post-perovskite and melt.

Table 1. Experimental Conditions and Results

Run	Pressure (GPa)	Temperature (K)[a]	Phase Assemblage in Crystallization Sequence[b]
#55	34	2900	Melt(58) → MgPv(34) → Fp(7) → CaPv(1)
#63	40	3000	Melt(74) → MgPv(23) → Fp(3) → CaPv(1)
#58	58	3600	Melt(77) → MgPv(21) → Fp(1) → CaPv(1)
#88	68	3900	Melt(61) → MgPv(30) → Fp(6) → CaPv(2)
#89	82	4000	Melt(51) → MgPv(39) → CaPv(3) → Fp(7)
#84	88	4000	Melt(47) → MgPv(40) → CaPv(4) → Fp(9)
#91	169	4900	Melt(49) → MgPP(40) → CaPv(3), Fp(7)
#90	179	5000	Melt(46) → MgPP(42) → CaPv(3), Fp(8)

[a]Inferred from the melting curves of peridotitic materials with the uncertainty of ±10%.
[b]MgPv, $MgSiO_3$-perovskite; Fp, ferropericlase; CaPv, $CaSiO_3$-perovskite; MgPP, $MgSiO_3$-post-perovskite. Number in parentheses are phase proportions (wt.%) calculated by mass balance.

2. Experimental Techniques

2.1. Melting Experiments at High Pressure

High-pressure melting experiments were conducted using laser-heated DAC techniques. A starting material was prepared originally from gel with a chemical composition of KLB-1 peridotite [*Takahashi*, 1986] with a primitive mantle composition similar to pyrolite, same as that used in *Sinmyo et al.* [2011] and *Sinmyo and Hirose* [2013]. The gels were dehydrated at 1273 K for 1 h in a H_2-CO_2 gas-mixing furnace, in which oxygen fugacity was controlled at 3 log units below the QFM buffer. The powder sample was pressed into a disc with a typical thickness of 15–25 μm and placed into a hole drilled at the center of a rhenium gasket that was pre-indented to a thickness of 25–40 μm. The sample may have included ~1000 ppm of adsorbed H_2O [*Nomura et al.*, 2014]. No additional metal laser absorber was used except for run #55, in which the sample disk was coated with iridium for both sides (200 nm thickness). Subsequently, liquid argon was loaded cryogenically as a pressure medium. The sample was compressed with beveled 120 and 150 μm or flat 300 μm culet diamond anvils, depending on a target pressure. Heating was performed from both sides of the sample by employing a 50 W donut-mode Nd:YLF laser or two 100 W single-mode Yb fiber lasers with beam

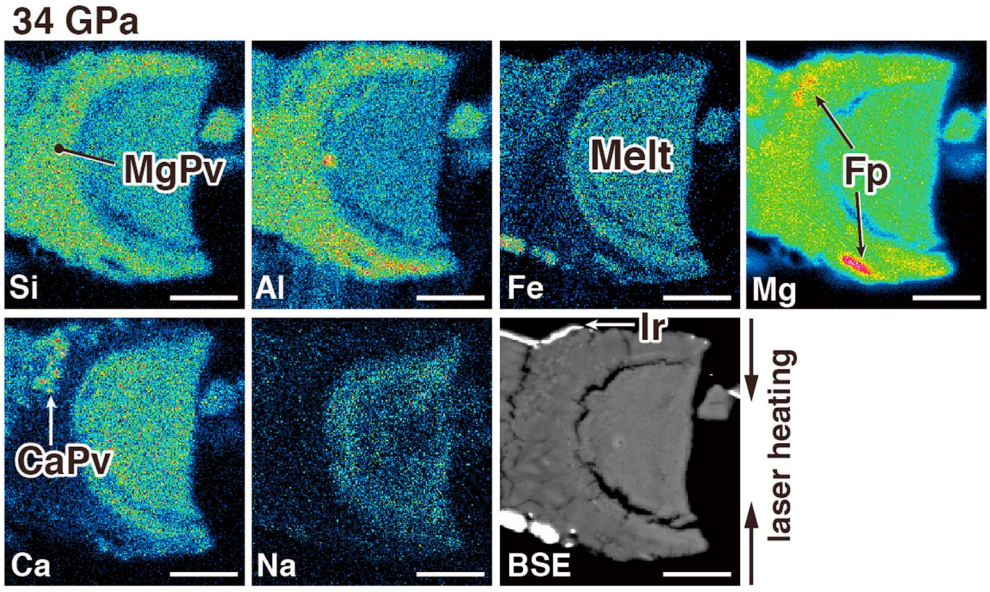

Figure 1. Backscattered electron (BSE) images and X-ray elemental maps for the sample recovered from 34 GPa (run #55). Quenched partial melt is found at the center of the sample, where temperature was the highest. Melt pocket is enclosed by a layer of single-phase $MgSiO_3$-perovskite (MgPv), the liquidus phase, followed by ferropericlase (Fp) and $CaSiO_3$-perovskite (CaPv). Iridium (Ir) was coated for both sides of the sample. Scale bar represents 5 μm. Arrows show the directions of laser beams for heating from both sides of the sample.

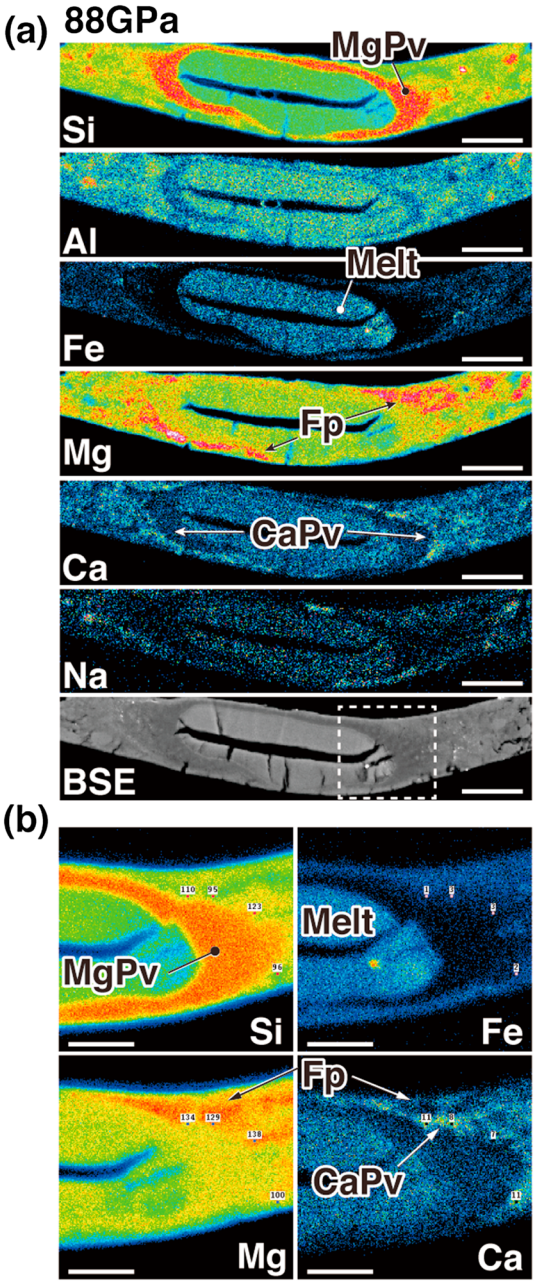

Figure 2. (a) Backscattered electron image and X-ray maps for the sample at 88 GPa (run #84), where $CaSiO_3$-perovskite (CaPv) is the second liquidus phase. MgPv, $MgSiO_3$-perovskite; Fp, ferropericlase. Scale bar, 10 μm. (b) Magnified X-ray maps for a boxed area in (a). Scale bar, 5 μm.

shaping optics converting a beam with a Gaussian intensity distribution to the one with a flat-top distribution. Temperature gradient in a melt pool would have been smaller than that in a solid part [*Nomura et al.*, 2014]. The laser spot size was about 20 to 30 μm on a sample. The sample was heated for about 1 s in order to avoid chemical segregation due to thermal diffusion under relatively large temperature gradient [*Sinmyo and Hirose*, 2010; *Nomura et al.*, 2011]. Sample temperature was not measured in this study because heating duration was too short, but alternatively it was estimated from melt fraction and the solidus and liquidus temperatures of peridotitic materials [*Fiquet et al.*, 2010; *Andrault et al.*, 2011], assuming that the degree of partial melting increases linearly with increasing temperature between the solidus and the liquidus [*Takahashi et al.*, 1993] (Table 1). Pressure was determined from the Raman peak shift of diamond anvil at 300 K after laser heating [*Akahama and Kawamura*, 2004] and corrected for a contribution (+20%) of thermal pressure at high temperature, which was estimated from previous in situ X-ray diffraction (XRD) measurements [*Ozawa et al.*, 2009; *Nomura et al.*, 2014].

2.2. Analytical Techniques

The textural and chemical characterizations were made on quenched samples. After complete pressure release, the sample was recovered from the DAC and glued on a silicon wafer using polymeric resin. Subsequently, it was polished by Ar ion beam using the Ion Slicer (JEOL EM-09100 IS) to minimize the damage of the sample surface [*Tateno et al.*, 2009], allowing us to observe the micro-textures of an extremely tiny sample. The section was carefully thinned to 10 μm such that the center of the heating spot was exposed from both sides parallel to the compression and laser-heating axis. Such polished sample section was examined under FE-EPMA (JEOL JXA-8500F) with an acceleration voltage of 10 kV and beam currents of 12 nA. We collected the X-ray mappings for Si, Ti, Al, Fe, Mg, Ca, and Na for each sample (Figures 1–3). The chemical compositions of quenched liquid pool and neighboring solid phase (perovskite or post-perovskite, depending on pressure) were obtained with defocused (5 μm size) and focused (<2 μm spatial resolution) beams, respectively (Table 2). Counting times were 20 s on the peak and 10 s on the background for each element. Because ferropericlase grains found in an Mg-rich portion were indeed too small, we estimated their compositions from the Fe/Mg ratio of coexisting $MgSiO_3$-rich perovskite (Table 2) using the Fe-Mg partition coefficient reported by *Sinmyo et al.* [2008]. Similarly, the composition of $CaSiO_3$ perovskite was assumed to be the same as that obtained by previous melting experiments on peridotite in a multi-anvil apparatus at 33 GPa [*Ito et al.*, 2004].

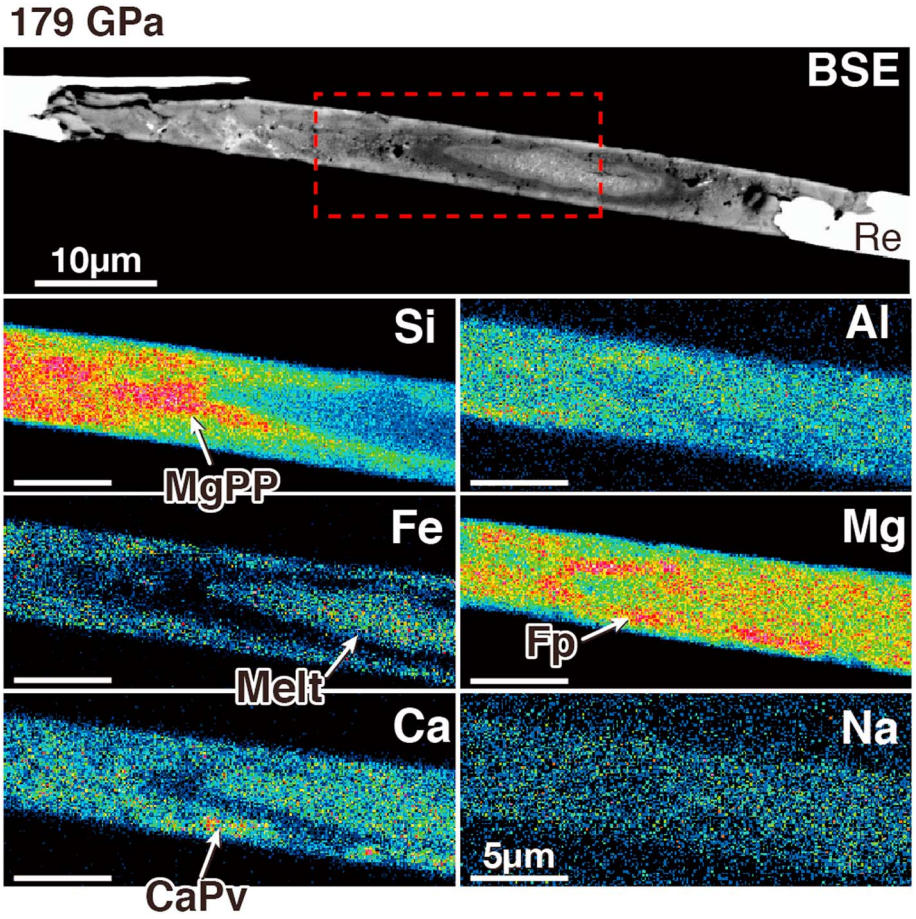

Figure 3. Backscattered electron images and X-ray maps for the sample at 179 GPa (run #90), in which post-perovskite (MgPP) is as a liquidus phase. CaPv, $CaSiO_3$-perovskite; Fp, ferropericlase.

Additionally, phase identification was made by synchrotron XRD measurements at BL10XU, SPring-8 in runs #90 and #91 [*Ohishi et al.*, 2008]. The XRD patterns were collected after laser heating on an imaging plate with an exposure time of 5 min. A monochromatic incident X-ray beam was focused by stacked compound refractive lenses and collimated to an approximately 6 μm area (full width of half maximum) on the sample. The wavelength used was 0.41415(7) Å (~30 keV). Visible fluorescence light from diamond excited by X-rays was used to precisely align the laser-heated spot with the X-ray beam. Two-dimensional XRD images were integrated as a function of two-theta angle in order to produce conventional one-dimensional diffraction pattern using the IP Analyzer program [*Seto et al.*, 2010].

3. Results

3.1. Melting Phase Relations

A total of nine separate experiments were performed at pressures ranging from 34 to 179 GPa. The melting sequence is indicated by textures (Figures 1–3, Table 1). The chemical compositions of partial melt and neighboring solid (liquidus phase) are given in Table 2, together with a proportion in weight % based on mass-balance calculations.

The sample recovered from 34 GPa (run #55) exhibited a concentric texture that reflected a temperature distribution during laser heating (Figure 1), similar to that observed in our previous melting experiments on $(Mg_{0.9}Fe_{0.1})_2SiO_4$ in a DAC [*Nomura et al.*, 2011]. A round pocket was found at the center, the hottest part of the sample, showing iron-rich non-stoichiometric composition. This should represent the quenched partial melt [*Andrault et al.*, 2012]. It is surrounded by an $MgSiO_3$-rich layer, corresponding to Mg-rich perovskite at

Table 2. Chemical Compositions of Quenched Melt and Coexisting Perovskite/Post-perovskite (wt.%)[a]

Run	P (GPa)	Phase	SiO_2	TiO_2	Al_2O_3	FeO[b]	MgO	CaO	Na_2O	Total[c]	K_D
#55	34	Melt	40.06 (0.54)	0.12 (0.04)	2.57 (0.14)	10.34 (0.54)	32.40 (0.57)	5.42 (0.34)	0.17 (0.05)	91.08 (0.73)	0.329 (0.025)
		MgPv	54.85 (1.62)	0.16 (0.08)	4.60 (0.28)	3.80 (0.19)	36.26 (0.53)	1.20 (0.27)	0.02 (0.01)	100.90 (1.69)	
#63	40	Melt	41.37 (1.20)	0.14 (0.09)	2.70 (0.12)	9.49 (0.86)	37.25 (2.15)	3.88 (1.03)	0.33 (0.08)	95.16 (2.33)	0.314 (0.055)
		MgPv	54.00 (1.35)	0.18 (0.04)	4.91 (0.42)	2.76 (0.38)	34.47 (0.57)	1.71 (0.54)	0.04 (0.02)	98.06 (0.88)	
#58	58	Melt	36.20 (3.21)	0.15 (0.08)	3.18 (0.26)	8.60 (1.17)	34.42 (1.69)	3.45 (0.34)	0.37 (0.15)	86.36 (4.84)	0.262 (0.059)
		MgPv	57.78 (1.92)	0.09 (0.06)	3.25 (0.17)	2.28 (0.39)	35.05 (0.79)	2.07 (0.22)	0.06 (0.03)	100.58 (2.36)	
#88	68	Melt	39.87 (0.99)	0.18 (0.06)	3.82 (0.11)	11.86 (0.85)	34.93 (1.22)	3.18 (0.15)	0.27 (0.03)	94.09 (1.43)	0.113 (0.020)
		MgPv	58.42 (0.86)	0.08(0.06)	2.16 (0.67)	1.33 (0.21)	34.64 (0.77)	2.42 (0.20)	0.06 (0.03)	99.11 (1.34)	
#89	82	Melt	39.44 (0.96)	0.21 (0.04)	4.18 (0.16)	14.53 (0.75)	35.89 (0.72)	3.34 (0.15)	0.34 (0.03)	97.94 (1.44)	0.106 (0.034)
		MgPv	58.94 (0.88)	0.08 (0.07)	2.94 (0.16)	1.46 (0.46)	34.19 (0.68)	2.64 (0.19)	0.08 (0.02)	100.32 (1.07)	
#84	88	Melt	38.63 (1.07)	0.23 (0.06)	4.19 (0.15)	15.50 (1.05)	33.53 (0.75)	3.22 (0.17)	0.27 (0.04)	95.57 (2.00)	0.085 (0.008)
		MgPv	59.79 (0.65)	0.04 (0.04)	2.72 (0.46)	1.37 (0.07)	34.96 (0.97)	2.33 (0.15)	0.07 (0.03)	101.28 (0.99)	
#91	169	Melt	37.55 (0.51)	0.16 (0.06)	3.78 (0.25)	15.44 (1.38)	34.17 (2.59)	3.67 (0.09)	0.26 (0.04)	95.03 (3.38)	0.037 (0.010)
		MgPP	59.37 (0.46)	0.07 (0.04)	2.56 (0.13)	0.59 (0.15)	35.49 (0.03)	1.63 (0.08)	0.08 (0.01)	99.79 (0.42)	
#90	179	Melt	37.85 (0.98)	0.23 (0.05)	3.82 (0.11)	16.00 (2.93)	33.49 (1.23)	3.45 (0.07)	0.33 (0.01)	95.17 (2.41)	0.042 (0.014)
		MgPP	58.62 (1.30)	0.06 (0.05)	2.61 (0.15)	0.70 (0.20)	34.98 (0.54)	1.62 (0.16)	0.09 (0.03)	98.67 (1.02)	

[a]Numbers in parentheses indicate one standard error.
[b]All Fe was assumed to be ferrous.
[c]Low totals for runs #55 and #58 may be attributed to the rough surface of quenched melt pools.

this pressure. We observed (Mg,Fe)O outside the $MgSiO_3$-rich perovskite layer, and $CaSiO_3$ further away from the center. Such zoning (phase segregation) has been commonly observed in conventional multi-anvil experiments and usually interpreted to show the crystallization sequence with decreasing temperature [e.g., *Trønnes and Frost*, 2002; *Hirose and Fei*, 2002; *Ito et al.*, 2004; *Liebske et al.*, 2005]. In this manner, the melting texture of the present DAC experiment at 34 GPa (Figure 1) demonstrates that Mg-rich perovskite is the liquidus phase, followed by the crystallizations of (Mg,Fe)O ferropericlase and then Ca-perovskite with decreasing temperature, which is in good agreement with the earlier melting experiments by the multi-anvil press on a peridotitic composition at 31–33 GPa [*Ito et al.*, 2004]. Similar melting texture was observed up to 68 GPa. *Fiquet et al.* [2010] found that ferropericlase remained a liquidus phase at 36 GPa. The difference from our results can be reconciled with the difference in the Mg/Si ratio of the sample; Mg/Si = 1.40 for the starting material used in *Fiquet et al.* [2010], whereas 1.31 for our sample. The higher Mg/Si ratio in the former experiments resulted in a wider stability of ferropericlase with respect to perovskite.

Above 82 GPa, the second liquidus phase changed from ferropericlase to Ca-perovskite) (Figure 2). As a result, the crystallization sequence was Mg-perovskite, Ca-perovskite, and then ferropericlase at 82 and 88 GPa. For the samples heated at 169 and 179 GPa, phase identification was made by XRD measurements at high pressures, in addition to microprobe analyses at ambient pressure. The XRD patterns obtained from a transparent zone adjacent to an opaque quenched melt pool showed the mineral assemblage of $CaIrO_3$-type post-perovskite + Ca-perovskite + ferropericlase (Figure 4) [*Murakami et al.*, 2005; *Ohta et al.*, 2008]. The X-ray elemental mappings of recovered samples exhibited that Fe-rich melt pool is present at the center and surrounded by a $MgSiO_3$-rich phase that should correspond to post-perovskite (Figure 3). The second liquidus phase is not clear in the present experiments at this pressure range.

3.2. Iron Partitioning Between Perovskite and Melt

The Fe-Mg distribution coefficient between perovskite/post-perovskite and melt, $K_D = ([\text{total Fe}^{\text{solid}}]/[\text{Mg}^{\text{solid}}])/([\text{total Fe}^{\text{melt}}]/[\text{Mg}^{\text{melt}}])$, was determined in the pressure range from 34 to 179 GPa (Table 2). We obtained $K_D = 0.329(30)$ at 34 GPa, consistent with the values obtained by earlier multi-anvil experiments on natural peridotite bulk compositions (0.402–0.460 at 26–33 GPa) (Figure 5a) [*Hirose and Fei*, 2002; *Ito et al.*, 2004; *Liebske et al.*, 2005]. The K_D value decreased with increasing pressure, reaching 0.113(20) at 68 GPa and 0.085(10) at 88 GPa, which indicates strong iron partitioning into partial melt. In particular, we found a precipitous change in K_D between 58 and 68 GPa, where it remarkably reduced from 0.262(60) to 0.113(20). The K_D between post-perovskite and melt was further low at 0.037–0.042.

3.3. Chemical Compositions of Coexisting Perovskite and Partial Melt

The chemical compositions of coexisting Mg-perovskite/post-perovskite and partial melt are given in Table 2, and their variations are illustrated as a function of pressure in Figure 6. We found systematic changes with increasing pressure, although the degree of partial melting ranged from 46 to 77 wt.% in the present experiments (Table 1).

The compositions of Mg-perovskite at 34 GPa are reasonably consistent with that obtained by multi-anvil experiment at 33 GPa [*Ito et al.*, 2004].

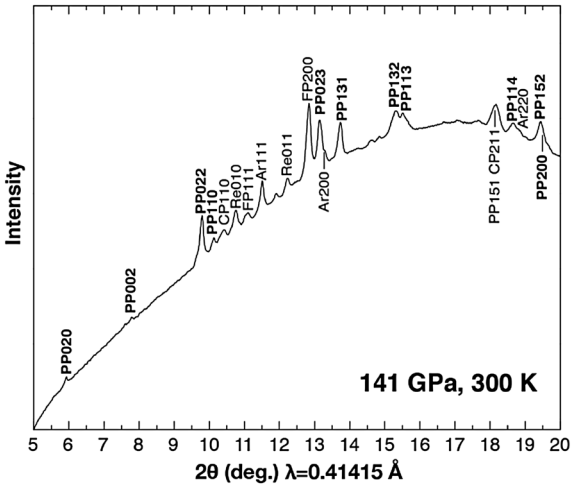

Figure 4. X-ray diffraction pattern of a pyrolitic mantle material obtained at 141 GPa and 300 K after melting (run #91). PP, post-perovskite; FP, ferropericlase; CP, $CaSiO_3$-perovskite; Ar, argon (pressure medium); Re, rhenium (gasket). $\lambda = 0.41415(7)$ Å.

The tetravalent cations, Si^{4+} and Ti^{4+}, sum up to a total of 0.93 when normalized to 3 oxygen, indicating that the octahedral site (B-site) is partially occupied by trivalent cations of Al^{3+} and Fe^{3+}. The presence of Fe^{3+} is supported by the fact that the total cations exceed 2. On the other hand, the Si^{4+} abundance in perovskite increased with increasing pressure and fully occupied the B-site above 68 GPa (Figure 6). Alternatively, Al^{3+} and Fe^{3+} impurities entered the A-site with the formation of cation vacancy, which is evidenced from the facts that (1) Mg^{2+} decreased with increasing pressure and (2) the total cation number decreased to less than 2 above 58 GPa. Indeed, the Al^{3+} content and likely the Fe^{3+} content in Mg-perovskite significantly reduced at higher pressures. As a consequence, Al^{3+} was incorporated more into melt rather than into perovskite above 58 GPa, while it was opposite below 40 GPa. In other words, Al^{3+} became incompatible to the B-site progressively with increasing pressure to 68 GPa.

Partial melts were ultrabasic in composition with less than 45 wt.% SiO_2 and more than 32 wt.% MgO (Table 2). The variations in the (Mg + Fe)/Si ratio of partial melt are illustrated as a function of pressure in Figure 7. The (Mg + Fe)/Si ratio was 1.42 at 34 GPa, very similar to that reported by the earlier multi-anvil experiment up to 33 GPa [*Hirose and Fei*, 2002; *Ito et al.*, 2004; *Liebske et al.*, 2005]. It increased to 1.6–1.7 with increasing pressure and then became almost constant above 80 GPa. Both TiO_2 and Al_2O_3 contents in melt increased with increasing pressure to around 80 GPa, consistent with the fact that they were less incorporated into the B-site of Mg-perovskite at higher pressures (Figure 6). The FeO (total Fe as FeO) content increased remarkably above 58 GPa, which contributed to the strong reduction in K_D in the relevant pressure range.

4. Discussion

4.1. Crystallization Sequence and Partial Melt Composition

Earlier melting experiments on peridotite and olivine bulk compositions have demonstrated that the first crystallizing phase (liquidus phase) changes from ferropericlase to Mg-perovskite above ~30 GPa [*Ito et al.*, 2004; *Fiquet et al.*, 2010; *Nomura et al.*, 2011]. Our results show that the liquidus phase is Mg-perovskite at 34 GPa and above (or post-perovskite in its stability field), in good agreement with these previous studies. *Ito et al.* [2004] observed that the liquidus phase converts between 29 and 31 GPa in a multi-anvil apparatus study. Such change in crystallization sequence is consistent with the present experimental results that the (Mg + Fe)/Si ratio in partial melt increased with increasing pressure (Figure 7).

Although melts obtained in this study were not eutectic melts but formed by certain degrees of partial melting, their variation in the (Mg + Fe)/Si ratio is broadly consistent with the change in eutectic composition in the MgO-$MgSiO_3$ binary system (Figure 7). Our data indicate that the (Mg + Fe)/Si ratio in partial melt of a pyrolitic mantle increased from 1.42 at 34 GPa to ~1.65 at about 80 GPa and remained nearly constant at higher pressures to 179 GPa. The thermodynamical modeling by *Liebske and Frost* [2012] based on their low-pressure experimental data demonstrated similar change in the Mg/Si ratio of eutectic melt composition in MgO-$MgSiO_3$. Present experimental results are also generally consistent with recent theoretical calculations on the MgO-$MgSiO_3$ system [*de Koker et al.*, 2013].

Present experiments also demonstrated that the second liquidus phase changed from ferropericlase to Ca-perovskite (in other words, the first melting phase changed from Ca-perovskite to ferropericlase) between

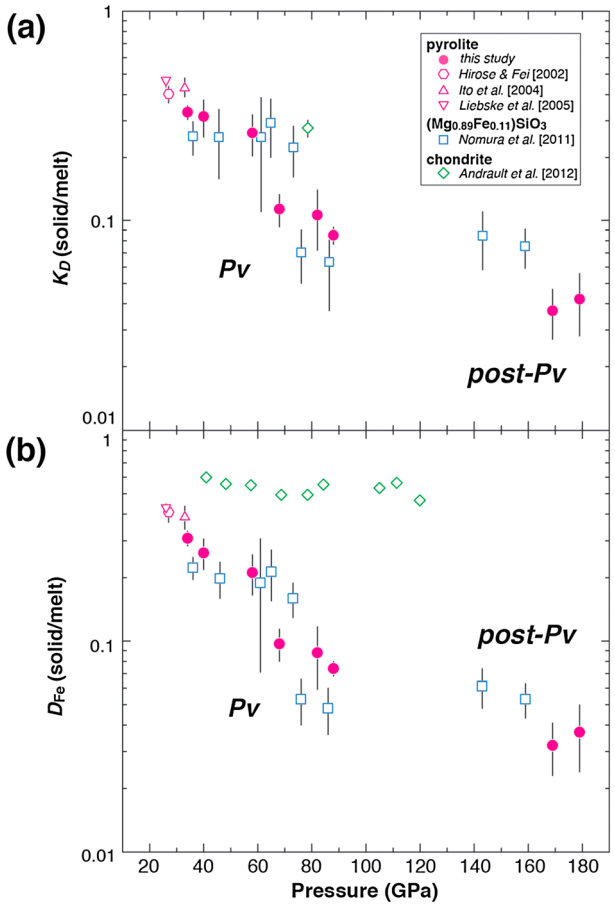

Figure 5. The change in Fe partitioning between perovskite/post-perovskite in a peridotitic bulk composition (red). Closed circles, this study; open symbols, previous multi-anvil experiments [*Hirose and Fei*, 2002; *Ito et al.*, 2004; *Liebske et al.*, 2005]. The results determined in $(Mg_{0.89}Fe_{0.11})_2SiO_4$ bulk composition (blue) [*Nomura et al.*, 2011] and in a chondritic mantle composition (green) [*Andrault et al.*, 2012] are also shown for comparison. Error was estimated from uncertainties (1σ) in both solid and liquid compositions. (a) Fe-Mg distribution coefficient, $K_D = ([Fe^{solid}]/[Mg^{solid}])/([Fe^{melt}]/[Mg^{melt}])$. The values decreased with increasing pressure with a drop between 58 and 68 GPa. All K_D data were based on the EPMA analysis of recovered samples. (b) Fe partition coefficients, $D_{Fe} = [Fe^{solid}]/[Fe^{melt}]$. The data by *Andrault et al.* [2012] were obtained from XRF analyses.

68 and 82 GPa (Table 1). It is consistent with the earlier DAC experiments combined with in situ XRD measurements on peridotite [*Fiquet et al.*, 2010], reporting that ferropericlase melted first at 61 GPa. It also agrees with the steep melting curve of Ca-perovskite compared to that of ferropericlase [*Zerr and Boehler*, 1994; *Zerr et al.*, 1997]. Such change certainly led to low CaO content in partial melts at higher pressures (Figure 6).

4.2. Iron Partitioning Between Perovskite and Melt

Present new data obtained in a natural mantle bulk composition show that the K_D value diminishes remarkably with increasing pressure, indicating strong Fe enrichment in partial melt in a deep lower mantle (Figure 5). These results are indeed in excellent agreement with our previous measurements of K_D in the $(Mg_{0.89}Fe_{0.11})_2SiO_4$ bulk composition using similar experimental techniques [*Nomura et al.*, 2011] (Figure 5a). Furthermore, a precipitous change in K_D is also found between 58 and 68 GPa, again similar to the results for the $(Mg_{0.89}Fe_{0.11})_2SiO_4$ bulk composition. These are possibly explained by the effect of iron spin crossover in melt as argued by *Nomura et al.* [2011]. On the other hand, such iron enrichment in partial melt may be related to the change in crystal chemistry of perovskite with increasing pressure described in section 3-3. The elevated silicon concentration in perovskite dismisses Al^{3+} and Fe^{3+} from the B-site and confines them into the A-site, which might enhance iron enrichment in coexisting partial melt.

In contrast, these results on iron partitioning contradict the recent experiments on a chondritic mantle bulk composition by *Andrault et al.* [2012]. Andrault and others observed small Fe-enrichment in partial melt with increasing pressure, but it was not as strong as those observed by *Nomura et al.* [2011] and in this study (Figure 5b). *Andrault et al.* [2012] determined the partition coefficient of iron, $D_{Fe} = [Fe^{Pv}]/[Fe^{melt}]$, between Mg-perovskite and quenched partial melt based on the synchrotron X-ray fluorescence (XRF) analyses. The D_{Fe} (not K_D) values obtained by Andrault and others are 0.5–0.6 over a wide pressure range of the lower mantle, much higher than ours (Figure 5b). They argued that the discrepancy could be explained by the difference in the bulk composition, in particular the presence/absence of Al_2O_3. However, our experiments on both Al-free [*Nomura et al.*, 2011] and Al-bearing bulk compositions [*this study*] show quite consistent results. Alternatively, a major source of the discrepancy is likely to be the difference in the method of chemical analysis. In their XRF analysis, the incident X-ray beam passes through a whole sample along the compression/heating axis (vertical direction in Figures 1–3). As clearly seen in our X-ray elemental maps of Fe (Figures 1–3), the quenched melt pocket is entirely surrounded by a "Fe-depleted" perovskite layer. Such Fe-depleted perovskite layer

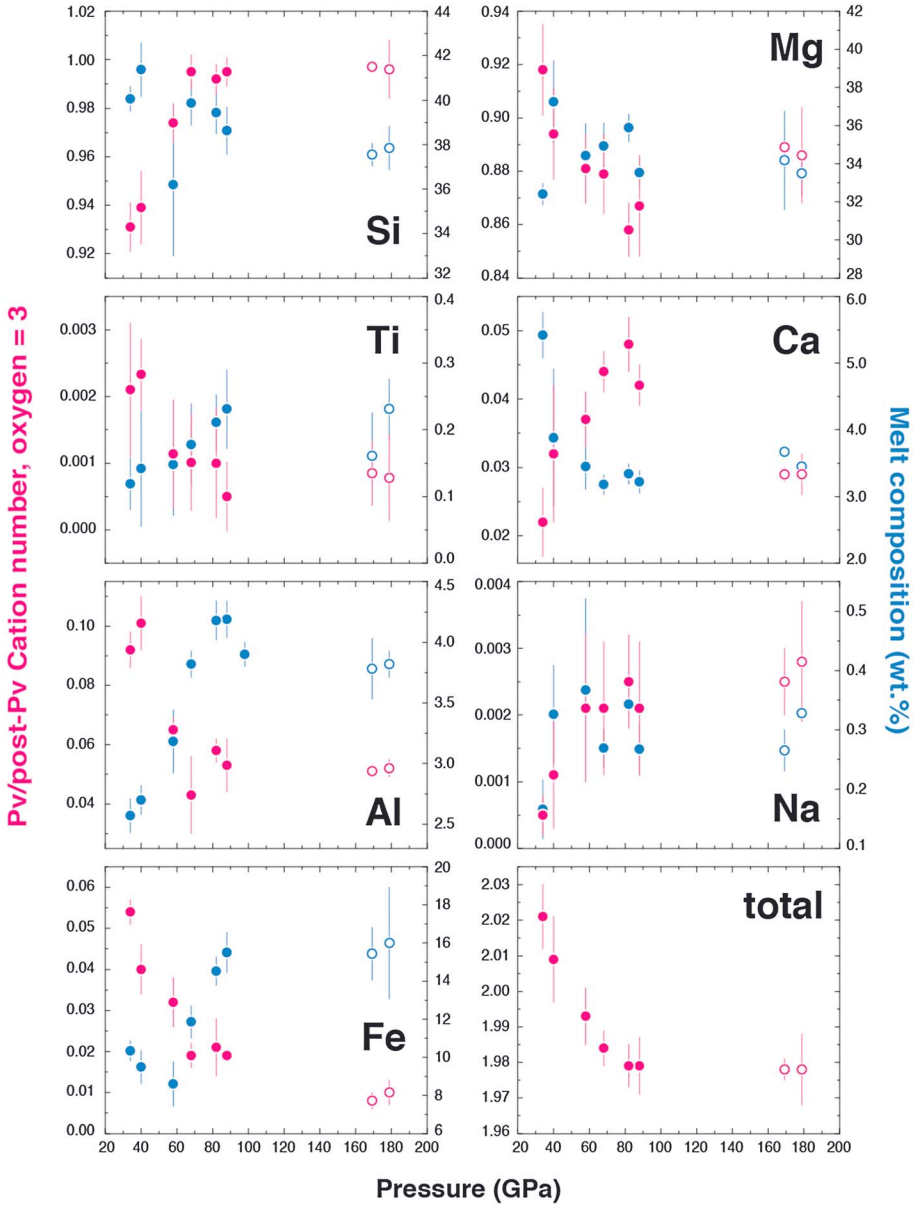

Figure 6. The variations in chemical compositions of coexisting $MgSiO_3$-perovskite/post-perovskite (left axis in cation number, red) and partial melt (right axis in weight %, blue) in a pyrolitic bulk composition as a function of pressure. Filled and open symbols indicate the data obtained in the stabilities of perovskite and post-perovskite, respectively.

always exists between the melt pocket and pressure medium. The X-ray fluorescence signals for partial melt, therefore, should have come from both quenched melt pocket and Fe-poor perovskite in *Andrault et al.* [2012]. On the other hand, the signals for perovskite also should have been contaminated by those from the unmelted part of the sample that was not depleted in Fe. Therefore, the XRF analyses underestimated and overestimated the Fe contents in partial melt and neighboring Mg-perovskite, respectively, leading to apparently high D_{Fe} values as observed by Andrault and others. It is also noted that *Andrault et al.* [2012] reported just one compositional datum for each perovskite and melt on the basis of microprobe analyses (see supporting information Table 2 in their paper). The K_D value at 79 GPa calculated from such microprobe data is in much better agreement with the present observations and indeed close to the results by *Nomura et al.* [2011] (Figure 5a).

In contrast, the chemical compositions of Mg-perovskite/post-perovskite and melt in this study as well as in *Nomura et al.* [2011] were obtained by electron microprobe analyses on quenched samples, using FE-EPMA

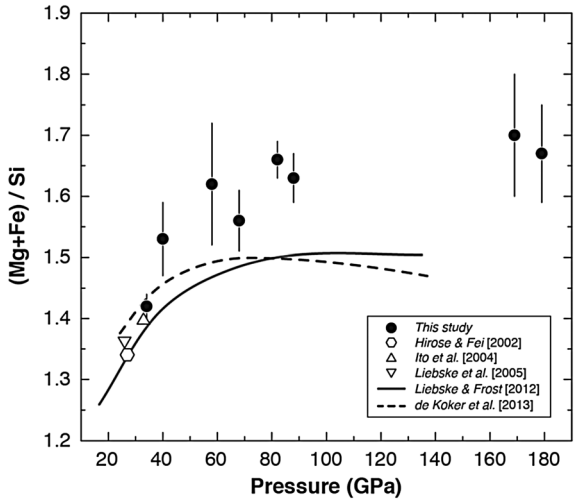

Figure 7. The variations in the (Mg + Fe)/Si molar ratio in partial melt as a function of pressure. Earlier multi-anvil experimental data obtained in a pyrolitic bulk composition are also shown [*Hirose and Fei*, 2002; *Ito et al.*, 2004; *Liebske et al.*, 2005]. Solid and dashed curves represent change in the Mg/Si ratio of eutectic melt composition in the MgO-$MgSiO_3$ binary system obtained by thermodynamic [*Liebske and Frost*, 2012] and ab initio [*de Koker et al.*, 2013] calculations, respectively.

with high spatial resolution. We prepared the cross section of a laser-heated hot spot in the sample and carefully examined the chemical compositions at the interface between solid and liquid phases under the microprobe (Figures 1–3).

4.3. Dense Partial Melt in the Deep Lower Mantle

Our experiments show that iron is progressively partitioned more into melts with increasing pressure in a natural pyrolitic lower mantle. Partial melts obtained in the present study contained more than 15 wt.% FeO above ~80 GPa corresponding to ~2000 km depth in the mantle. While they were formed by 46–77 % partial melting (Table 1), melts should be more enriched in FeO at lower degrees of partial melting, because (Mg,Fe)O ferropericlase is the first phase to melt near the solidus temperature above 82 GPa.

Since melt has higher compressibility than solid, the volume of melt becomes closer to that of solid at high pressure. While theory suggested that melt is still buoyant relative to solid of the same chemical composition even at the base of the mantle [*Stixrude and Karki*, 2005], the addition of heavy elements such as iron and calcium to a system further decreases the density contrast [*Stixrude et al.*, 2009; *Sun et al.*, 2011].

The partitioning of iron between perovskite and melt primarily controls the buoyancy of partial melt in the lower mantle, although the Mg/Si ratio also plays some role [*Funamori and Sato*, 2010; *Thomas et al.*, 2012]. *Nomura et al.* [2011] argued that the K_D value of 0.1 and smaller makes partial melt denser than any typical lower mantle minerals. *Funamori and Sato* [2010] and *Thomas et al.* [2012] demonstrated a sink/float relationship between perovskite and melt as functions of Mg/(Mg + Fe) and SiO_2 content in melt. According to the former model using static compression data, partial melt formed at or greater than 88 GPa is denser than the surrounding solid mantle (Figure S1a in the supporting information). The latter model can be applied only at 135 GPa, indicating that the partial melt at the bottom of the mantle is denser than $MgSiO_3$ perovskite (Figure S1b). All of these indicate that perovskite-melt density crossover may occur above 88 GPa corresponding to about 2000 km depth.

Additionally, *Thomas et al.* [2012] also obtained the equation of state of liquid Fe_2SiO_4 from shock-wave experiments and calculated the isentrope for liquid KLB-1 peridotite, which is tangent to its liquidus temperature at 85 GPa. These results suggest that a deep magma ocean would have started crystallization around 2000 km, and melt was gravitationally stable underneath a solidified layer. Note that the melt became denser in a later stage of solidification [*Thomas et al.*, 2012] because it was progressively richer in FeO and poorer in SiO_2 [*Nomura et al.*, 2011].

5. Summary and Conclusions

Melting phase relations and chemical compositions of coexisting perovskite (or post-perovskite) and melt were experimentally determined in a pyrolitic mantle bulk composition over the entire lower mantle pressure range. The degree of partial melting ranged from 46 to 77 wt.% in this study. The liquidus phase changed from (Mg,Fe)O ferropericlase to $MgSiO_3$-rich perovskite at least above 34 GPa. The last crystallizing phase (the first melting phase) also changed from $CaSiO_3$ perovskite to ferropericlase between 68 and 82 GPa. These led to the change in partial melt composition; melt became more depleted in SiO_2 and more enriched in FeO (total Fe) with increasing pressure. We also found that the B-site of Mg-perovskite was fully occupied by

Si above 68 GPa and Al^{3+} was likely to be incorporated only into the A-site with cation vacancy in the presence of partial melt. As a result, Al^{3+} is partitioned more into partial melt than into Mg-perovskite above ~50 GPa.

The Fe-Mg distribution coefficients (K_D) between perovskite and melt remarkably decreased with increasing pressure, with a precipitous reduction at ~60 GPa, which is quite consistent with earlier experiments performed in $(Mg,Fe)_2SiO_4$ bulk composition [*Nomura et al.*, 2011]. It is, however, contradictory to those obtained in more recent work based on the XRF measurements [*Andrault et al.*, 2012], and the discrepancy is attributed to the difference in the analytical method. The K_D values determined in this study indicate strong iron-enrichment in partial melt in a deep lower mantle. On the basis of the liquid equation of state recently proposed by *Thomas et al.* [2012], melt was negatively buoyant and gravitationally stable at depths greater than 2000 km in a deep magma ocean.

Acknowledgments

We thank N. Hirao, H. Shukuno, and Y. Tatsumi for their technical assistance. The gel starting material was kindly provided by R. Sinmyo. The manuscript was further improved by the comments and suggestions of the editor and two anonymous reviewers. The synchrotron X-ray diffraction measurements were conducted at BL10XU of SPring-8 (proposal no. 2011A0087). Data for a sink/float relationship is available as in supporting information Figure S1.

References

Akahama, Y., and H. Kawamura (2004), High pressure Raman spectroscopy of diamond anvils to 250 GPa: Method for pressure determination in the multimegabar pressure range, *J. Appl. Phys.*, *96*, 3748–3751, doi:10.1063/1.1778482.

Andrault, D., N. Bolfan-Casanova, G. Lo Nigro, M. A. Bouhifd, G. Garbarino, and M. Mezouar (2011), Solidus and liquidus profiles of chondritic mantle: Implication for melting of the Earth across its history, *Earth Planet. Sci. Lett.*, *304*, 251–259, doi:10.1016/j.epsl.2011.02.006.

Andrault, D., S. Petitgirard, G. Lo Nigro, J.-L. Devidal, G. Veronesi, G. Garbarino, and M. Mezouar (2012), Solid-liquid iron partitioning in Earth's deep mantle, *Nature*, *487*, 354–357, doi:10.1038/nature11294.

Canup, R. M. (2004), Simulation od a late lunar-forming impact, *Icarus*, *168*, 433–456, doi:10.1016/j.icarus.2003.09.028.

de Koker, N., B. B. Karki, and L. N. Stixrude (2013), Thermodynamics of the MgO–SiO_2 liquid system in Earth's lowermost mantle from first principles, *Earth Planet. Sci. Lett.*, *361*, 58–63, doi:10.1061/j.epsl.2012.11.026.

Fiquet, G., A. L. Auzende, J. Siebert, A. Corgne, H. Bureau, H. Ozawa, and G. Garbarino (2010), Melting of peridotite to 140 gigapascals, *Science*, *329*, 1516–1518, doi:10.1126/science.1192448.

Funamori, N., and T. Sato (2010), Density contrast between silicate melts and crystals in the deep mantle: An integrated view based on static-compression data, *Earth Planet. Sci. Lett.*, *295*, 435–440, doi:10.1016/j.epsl.2010.04.021.

Garnero, E. J., and D. V. Helmberger (1995), A very slow basal layer underlying large-scale low-velocity anomalies in the lower mantle beneath the Pacific: Evidence from core phases, *Phys. Earth Planet. Inter.*, *91*, 161–176, doi:10.1016/0031-9201(95)03039-Y.

Hirose, K., and Y. Fei (2002), Subsolidus and melting phase relations of basaltic composition in the uppermostlower mantle, *Geochim. Cosmochim. Acta*, *66*, 2099–2108, doi:10.1061/S0016-7037(02)00847-5.

Hirose, K., N. Shimizu, W. van Westrenen, and Y. Fei (2004), Trace element partitioning in Earth's lower mantle and implications for geochemical consequences of partial melting at the core–mantle boundary, *Phys. Earth Planet. Inter.*, *146*, 249–260, doi:10.1061/j.pepi.2002.11.001.

Ito, E., A. Kubo, T. Katsura, and M. J. Walter (2004), Melting experiments of mantle materials under lower mantle conditions with implications for magma ocean differentiation, *Phys. Earth Planet. Inter.*, *143–144*, 397–406, doi:10.1016/j.pepi.2003.09.016.

Labrosse, S., J. W. Hernlund, and N. Coltice (2007), A crystallizing dense magma ocean at the base of the Earth's mantle, *Nature*, *450*, 866–869, doi:10.1038/nature06355.

Lay, T., E. J. Garnero, and Q. Williams (2004), Partial melting in a thermo-chemical boundary layer at the base of the mantle, *Phys. Earth Planet. Inter.*, *146*, 441–467, doi:10.1016/j.pepi.2004.04.004.

Liebske, C., and D. J. Frost (2012), Melting phase relations in the MgO–$MgSiO_3$ system between 16 and 26 GPa: Implications for melting in Earth's deep interior, *Earth Planet. Sci. Lett.*, *345–348*, 159–170, doi:10.1016/j.epsl.2012.06.038.

Liebske, C., A. Corgne, D. J. Frost, D. C. Rubie, and B. J. Wood (2005), Compositional effects on element partitioning between Mg-silicate perovskite and silicate melts, *Contrib. Mineral. Petrol.*, *149*, 113–128, doi:10.1007/s00410-004-0641-8.

Mosenfelder, J. L., P. D. Asimow, D. J. Frost, D. C. Rubie, and T. J. Ahrens (2009), The $MgSiO_3$ system at high pressure: thermodynamic properties of perovskite, postperovskite, and melt from global inversion of shock and static compression data, *J. Geophys. Res.*, *114*, B01203, doi:10.1029/2008JB005900.

Murakami, M., K. Hirose, N. Sata, and Y. Ohishi (2005), Post-perovskite phase transition and mineral chemistry in the pyrolitic lowermost mantle, *Geophys. Res. Lett.*, *32*, L03304, doi:10.1029/2004GL021956.

Nomura, R., H. Ozawa, S. Tateno, K. Hirose, J. Hernlund, S. Muto, H. Ishii, and N. Hiraoka (2011), Spin crossover and iron-rich silicate melt in the Earth's deep mantle, *Nature*, *473*, 199–202, doi:10.1038/nature09940.

Nomura, R., K. Hirose, K. Uesugi, Y. Ohishi, A. Tsuchiyama, A. Miyake, and Y. Ueno (2014), Low core-mantle boundary temperature inferred from the solidus of pyrolite, *Science*, *343*, 522–525, doi:10.1126/science.1248186.

Ohishi, Y., N. Hirao, N. Sata, K. Hirose, and M. Takata (2008), Highly intense monochromatic X-ray diffraction facility for high-pressure research at SPring-8, *High Pressure Res.*, *28*, 163–173, doi:10.1080/08957950802208910.

Ohta, K., K. Hirose, T. Lay, N. Sata, and Y. Ohishi (2008), Phase transitions in pyrolite and MORB at lowermost mantle conditions: Implications for a MORB-rich pile above the core–mantle boundary, *Earth Planet. Sci. Lett.*, *267*, 107–117, doi:10.1016/j.epsl.2007.11.037.

Ozawa, H., K. Hirose, M. Mitome, Y. Bando, N. Sata, and Y. Ohishi (2009), Experimental study of reaction between perovskite and molten iron to 146 GPa and implications for chemically distinct buoyant layer at the top of the core, *Phys. Chem. Miner.*, *36*, 355–363, doi:10.1007/s00269-008-0283-x.

Seto, Y., D. Nishio-Hamane, T. Nagai, and N. Sata (2010), Development of a software suite on X-ray diffraction experiments, *Rev. High Pressure Sci. Technol.*, *20*, 269–276.

Sinmyo, R., and K. Hirose (2010), The Soret diffusion in laser-heated diamond-anvil cell, *Phys. Earth Planet. Inter.*, *180*, 172–178, doi:10.1016/j.pepi.2009.10.011.

Sinmyo, R., and K. Hirose (2013), Iron partitioning in pyrolitic lower mantle, *Phys. Chem. Miner.*, *40*, 107–113, doi:10.1007/s00269-012-0551-7.

Sinmyo, R., K. Hirose, D. Nishio–Hamane, Y. Seto, K. Fujino, N. Sata, and Y. Ohishi (2008), Partitioning of iron between perovskite/postperovskite and ferropericlase in the lower mantle, *J. Geophys. Res.*, *113*, B11204, doi:10.1029/2008JB005730.

Sinmyo, R., K. Hirose, S. Muto, Y. Ohishi, and A. Yasuhara (2011), The valence state and partitioning of iron in the Earth's lowermost mantle, *J. Geophys. Res.*, *116*, B07205, doi:10.1029/2010JB008179.

Stixrude, L., and B. Karki (2005), Structure and freezing of $MgSiO_3$ liquid in Earth's lower mantle, *Science*, *310*, 297–299, doi:10.1126/science.1116952.

Stixrude, L., N. de Koker, N. Sun, M. Mookherjee, and B. B. Karki (2009), Thermodynamics of silicate liquids in the deep Earth, *Earth Planet. Sci. Lett.*, *278*, 226–232, doi:10.1061/j.epsl.2008.12.006.

Sun, N., L. Stixrude, N. de Koker, and B. B. Karki (2011), First principles molecular dynamics simulations of diopside ($CaMgSi_2O_6$) liquid to high pressure, *Geochim. Cosmochim. Acta*, *75*, 3792–3802, doi:10.1016/j.gca.2011.04.004.

Takahashi, E. (1986), Melting of a dry peridotite KLB-1 up to 14 GPa: implications on the origin of peridotitic upper mantle, *J. Geophys. Res.*, *91*, 9367–9382, doi:10.1029/JB091iB09p09367.

Takahashi, E., T. Shimazaki, Y. Tsuzaki, and H. Yoshida (1993), Melting study of peridotite KLB–1 to 6.5 GPa and the origin of basaltic magmas, *Philos. Trans. R. Soc. London A*, *342*, 105–120.

Tateno, S., R. Sinmyo, K. Hirose, and H. Nishioka (2009), The advanced ion milling method for preparation of thin film using Ion Slicer: Application to a sample recovered from diamond-anvil cell, *Rev. Sci. Instrum.*, *80*, 013901, doi:10.1063/1.3058760.

Thomas, C. W., Q. Liu, C. B. Agee, P. D. Asimow, and R. A. Lange (2012), Multi-technique equation of state for Fe_2SiO_4 melt and the density of Fe-bearing silicate melts from 0 to 161 GPa, *J. Geophys. Res.*, *117*, B10206, doi:10.1029/2012JB009403.

Trønnes, R. G., and D. J. Frost (2002), Peridotite melting and mineral-melt partitioning of major and minor elements at 22–24.5 GPa, *Earth Planet. Sci. Lett.*, *197*, 117–131, doi:10.1061/S00127-821X(02)004667-1.

Walter, M. J., E. Nakamura, R. G. Trønnes, and D. J. Frost (2004), Experimental constraints on crystallization differentiation in a deep magma ocean, *Geochim. Cosmochim. Acta*, *68*, 4267–4284, doi:10.1016/j.gca.2004.03.014.

Zerr, A., and R. Boehler (1994), Constraints on the melting temperature of the lower mantle from high-pressure experiments on MgO and magnesiowustite, *Nature*, *371*, 506–508, doi:10.1038/371506a0.

Zerr, A., G. Serghiou, and R. Boehler (1997), Melting of $CaSiO_3$ perovskite to 430 kbar and first in-situ measurements of lower mantle eutectic temperatures, *Geophys. Res. Lett.*, *24*, 909–912, doi:10.1029/97GL00829.

Zhang, J., and C. Hertzberg (1994), Melting experiments on anhydrous peridotite KLB-1 from 5.0 to 22.5 GPa, *J. Geophys. Res.*, *99*, 17,729–17,742, doi:10.1029/94JB01406.